Robust Chiral Organization of Cellulose Nanocrystals in Capillary Confinement

*V. Cherpak [a], V.F. Korolovych [a], R. Geryak [a], T. Turiv [b], D. Nepal [c], J. Kelly [c], T. J. Bunning [c], O.D. Lavrentovich [b,d], W. T. Heller[e], V.V. Tsukruk [a] **

[a]School of Materials Science and Engineering, Georgia Institute of Technology, Atlanta, Georgia 30332, USA
[b]Liquid Crystal Institute and Chemical Physics Interdisciplinary Program, Kent State University, Kent, OH, 44240, USA
[c]Air Force Research Laboratory, Materials and Manufacturing Directorate, Wright Patterson Air Force Base, OH, 45433, USA
[d]Department of Physics, Kent State University, Kent, OH, 44240, USA
[e]Neutron Scattering Division, Oak Ridge National Laboratory, Oak Ridge, Tennessee 37831, USA

* Corresponding Author E-mail: vladimir@mse.gatech.edu

ABSTRACT

We showed large area uniformly aligned chiral photonic bioderived films from a liquid crystal phase formed by a cellulose nanocrystal (CNC) suspension placed in a thin capillary. As a result of the spatial confinement of the drying process, the interface between coexisting isotropic and chiral phases aligns perpendicular to the long axis of the capillary. This orientation facilitates a fast homogeneous growth of chiral pseudo-layers parallel to the interface. Overall, formation of organized solids takes hours vs. weeks in contrast to the slow and heterogeneous process of drying from the traditional dish-cast approach. The saturation of water vapor in one end of the capillary causes anisotropic drying and promotes unidirectional propagation of the anisotropic phase in large regions that results in chiral CNC solid films with uniformly oriented layered morphology. Corresponding ordering processes were monitored *in-situ* at nanoscale, mesoscale, and microscopic scale with complementary scattering and microscopic techniques. The resulting films show high orientation order at multi-length scale over large regions and preserved chiral handedness causing a narrower optical reflectance band and uniform birefringence over macroscopic regions in contrast to traditional dish-cast CNC films and those assembled in magnetic field and on porous substrates. These thin films with controllable and well-identified uniform morphology, structural colors and handedness open up interesting possibilities for broad applications in bio-derived photonic nanomaterials.

KEYWORDS: cellulose nanocrystals, liquid crystal phase, chiral nematic formation, real-time monitoring

INTRODUCTION

Cellulose nanocrystals (CNC) with high aspect ratio are suggested as a promising functional bio-derived material due in part to their inherent ability to form chiral phases with brilliant structural colors.[1,2] Despite the enormous potential, large-scale uniform alignment of CNCs with uniform ordering over large regions and well-controlled biophotonic properties remains a significant challenge.[3,4,5] Large-scale uniform alignment of these colloidal nanocrystals in the chiral cholesteric phase remains elusive. Large degrees of non-uniformity and random orientation in the liquid crystal (LC) structure leads to high levels of broad light scattering in the reflection spectrum, limiting the usefulness of such films. Drop casting from a concentrated aqueous suspension is the typical method for producing chiral films from CNC materials. The method typically results in poorly-controlled coffee ring structures with heterogeneous regions due to complex balance of wetting, flow, and drying processes.[6,7,8,9,10,11]

The central colloidal organization of an individual chiral domain (tactoid) is independently controlled by the respective director at the interface and the twisting tendency of the chiral director. The CNCs and the director of the chiral phase align parallel to the isotropic-liquid crystal interface within the bulk of any domain,[12,13] yet along the two-phase interface, the inner director deforms due to the curved surface of the domain.[13] As a result, coalescence of randomly oriented chiral droplets with very few curved layers (so called pseudo-layers [4]) results in a polydomain texture with random orientation of the director and numerous defects such as disclinations and dislocations.[14,15,16,17,18,19] Further drying of the LC suspension produces other sources of defects including non-uniform accumulation of material at the edge of drying droplets caused by “stick-slip” motion of the receding liquid front and Marangoni flow.[20,21,22,23,24,25] Complex drying profiles have been used to “anneal” tactoids into larger domains, but such methods require long times and still produce a patchy surface (though with remarkably increased patch size).[26] A few attempts to fabricate uniform CNC films by shearing has yielded only modest success due to rheological instabilities.[27,28,29] In contrast, the impact of confined geometry on LC alignment was promising for stand-alone CNC LC droplets[30] and magnetic fields have been shown to cause higher alignment in macroscale films[31]. The oriented films have been obtained by Chen et al via vacuum-

assisted filtration of the CNC suspensions.[32] These approaches demonstrate that the alignment of CNCs during drying can greatly improve the homogeneity of the films, which leads to improved control over reflectivity and can be beneficial for further design of lightweight tough with uniform chiral morphology.

In this work, uniformly aligned chiral CNC materials [33] are demonstrated by controlling the geometry of isotropic-liquid crystal interface under confined drying conditions within thin capillaries (Fig. 1). This confinement enables tight control of fast and uniform birefringent CNC film formation across macroscopically significant regions with uniformly oriented layered morphology across multiple length scales and narrow optical reflection bands.

RESULTS AND DISCUSSION

The method exploited in this work utilizes a thin wall rectangular (50 μm height, width 1mm) capillary which is filled with an isotropic CNC suspension via wetting-induced upward flow (Fig. 1a and see Scheme S1 and SI for more details). In this design, the slow evaporation at the top meniscus (open-edge) by the presence of the saturated vapor, combined with fast water evaporation at the bottom, causes asymmetric drying of the concentrated suspension and its flow to the pinned interface right after pulling capillary out (Fig. 1b).[18,34,35]

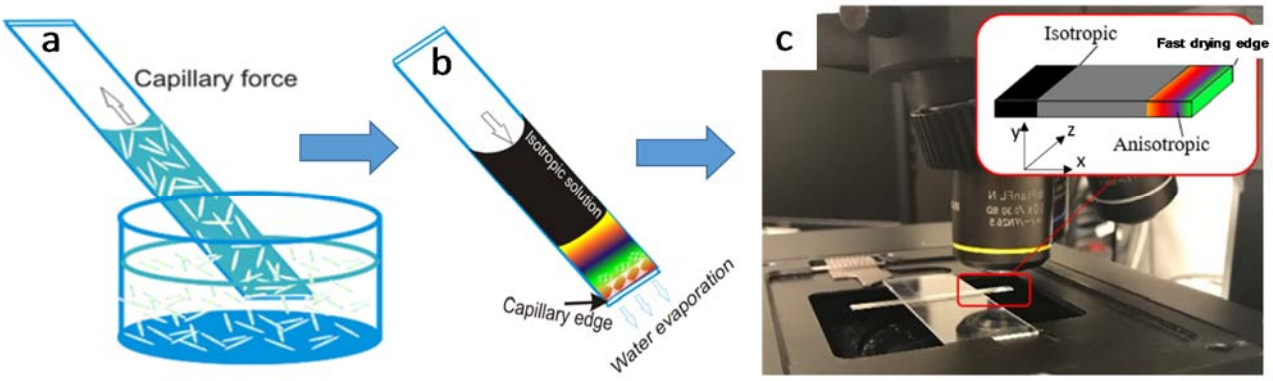

Figure 1. Filling of rectangular capillary with CNC suspension (a), pulling out capillary (b) and immediately transferring to optical stage for real-time monitoring of the LC phase formation process (c). XYZ orientation coordinates of the rectangular capillary formation process, which is referred for different images discussed below.

Because of the partial filling of the capillary, the side of the capillary containing air evaporates at slower rate than the filled side, which leads to symmetry breaking and the fast formation of an LC film at the fast evaporation side (the “Fast Drying Edge” in Fig. 1c). Slow

drying (several hours) allows for transfer of the suspension-filled capillary to the microscopic stage in a strictly horizontal position under optical objective (Fig. 1c). After setting the capillary into a horizontal position within a minute, the LC film assembly occurs without any further steps needed to ensure slow uniform film formation (Videos S1-S4). Moreover, the LC phase formation can be monitored in real-time at a nanoscale (with small-angle neutron scattering) and a microscopic scale (with cross-polarized microscopy, birefringence mapping and fluorescent confocal microscopy) with the solid state morphology after the film formation finally studied at mesoscale with electron and force microscopies. It is worth to note that in this report, we focus on one type of capillary environment and a number of other confined conditions (round capillary, different dimensions, concentrations, and CNC types) were preliminary tested in order to monitor film formation (see details in SI). Overall, general trends and final morphologies were similar to those reported here but the elucidation of the fine role of the specific confined conditions and the capillary walls of fine morphological features goes beyond the scope of the current work.

This preferential one-sided water evaporation causes unidirectional suspension flow towards the filling end with initial solidification of CNCs and uniform orientation along the x-axis (Fig. 1c). This in-situ microscopy views the CNC dispersion along the y-axis in Fig. 1c. Furthermore, capillary-guided drying takes only few hours (from 2 to 8 depending on fill height) to form uniform solid films which compares very favorably to dish-cast methods that requires slow drying (sometimes on the order of weeks).[36,37] Finally, a minimum contribution from gravity during process monitoring is facilitated by fast (seconds) horizontal alignment of the capillary immediate after initial filling.

As the chiral anisotropic phase forms as a result of increasing suspension concentration, layered birefringent regions form with preferential orientation of chiral pseudo-layers parallel to the isotropic-liquid crystal interface with a large pitch size clearly visible in optical images at different stages of the formation(Figs. 2a, b). Precise pitch size can be calculated from birefringence profile of the retardation map (Fig. 4c, see red line in Fig. S4d). For example, at particular stage captured in Fig.4c, the pitch size varies from 8.5 μm in the vicinity of the drying edge to 20 μm in the vicinity of isotropic-LC region (blue line in Fig. 4d).

Under these conditions, the rod-like cellulose nanocrystals align along the pinned bottom interface (Fig. 2b).[38,39] Further water evaporation results in increased suspension concentration and the fast appearance of a highly birefringent anisotropic phase with densely stacked layers apparent in higher resolution microscopic images (Fig. 2e, f; see below). Furthermore, it is expected that the final stages of drying initiate a further, directed compression that serves to align and shrink the domains in the films.[40]

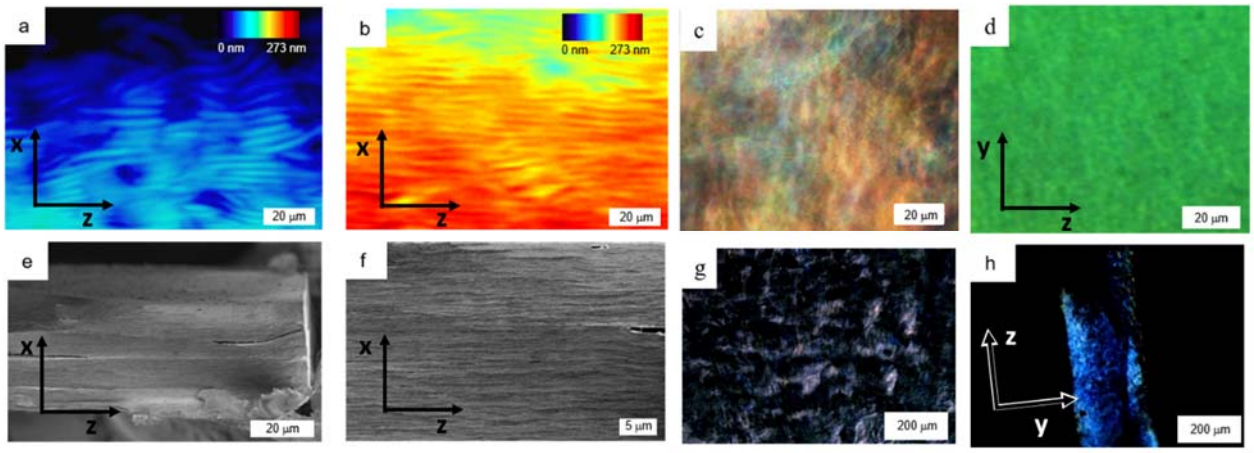

Figure 2. Optical birefringence of the anisotropic phase in concentrated CNC dispersion during LC phase formation process (a) and dried (b) solid capillary-formed film; birefringence increasing when color changes from blue to red. Cross-polarized optical microscopy images from dish-cast (c) and capillary-formed (d) CNC films. SEM images of the capillary-formed CNC films at different magnifications (e, f). Image subtraction, left circular analyzer – right circular analyzer for dish-cast (g) and capillary-formed (h) films. Note that a, b, e, and f are viewed along the y-axis of capillary whereas d and h are viewed along the x-axis of capillary (see axis orientations in images and Scheme S1).

The cross-polarized images of the films show a patchy heterogeneous structure for the dish-cast films and a mono-domain structure over hundred microns regions for the capillary dried films (Fig. 2c,2d). Note that in both cases, the image plane is perpendicular to the primary drying direction for the films. The microdomain nature of the dish-cast films can be seen by comparing left and right circular polarization images (Figs. 2g ,S2a, and S2b).[9] In contrast, the films dried in capillaries show large areas that uniformly reflect left circularly polarized light (Fig. 2h, S2c and S2d). This indicates a preservation of the CNC handedness and an enhancement of the chiral reflection from such films, which in turn, has been correlated to uniformity in the tilt of the chiral domains.[31] Scanning electron microscopy (SEM) and atomic force microscopy (AFM) images of thoroughly dried rectangular CNC solid films unambiguously confirm uniform and consistent layered morphology across the entire film thickness oriented parallel to the capillary edge (Fig. 2e,

f, Fig. S1). It is worth to mention that structured surfaces might significantly improve to uniformity of the films under regular casting conditions, we speculate that the absence of the uniform, unidirectional flow during confined drying will compromise the final film homogeneity.

Moreover, the kinetics of the chiral LC structure formation during the drying process was captured in *real-time* using polarized optical microscopy, retardation mapping, and small-angle neutron scattering at nanoscale (Fig. 3 and Figs. S4-S6). First, Fig. 3a-e shows selected optical frames of the different stages, and the corresponding ordering process is schematically shown in Fig. 3f-j. The pinned air-solid interface serves as a substrate-free support for the LC phase (Fig. 3a and Videos S1, S2). The initial preferential orientation of the LC layered structure is caused by the spontaneous capillary-driven alignment of the rod-like individual nanocrystals at the liquid-air interface. *In situ* SANS data also demonstrates that a partially aligned CNC phase emerges at this interface after 10 minutes of LC phase formation (see discussion below, Fig. S7, Video S5).[41]

Consequently, below the top meniscus, the isotropic-anisotropic liquid interface is formed quickly followed by birefringent LC phase formation due to the unidirectional flow to the bottom air-liquid interface (Fig. 3b, 3g, S4, S5, S6, Videos S1, S2). The initial height of the total suspension volume (isotropic and anisotropic) was 25 mm and gradually diminished. The anisotropic lyotropic LC phase is further compressed by the moving meniscus towards the bottom interface at later stages of drying (Fig. 3c, 3h, and Fig. S5a). At the final stage of the chiral LC phase formation, an approaching top meniscus promotes fast shrinkage of the suspension volume and a sharp increase of the local CNC concentration resulting in rapid (last 5% of the total time) formation of the uniform anisotropic phase possessing birefringence (Fig. 3d, 3e, 3l, 3j and Videos S2, S3). Similar temporal dynamics the LC phase formation was observed in the case of a round capillary (Video S4). The ultimate compaction of the LC domains during the final stages of the drying process likely occurs in a manner similar to the interface-driven uniaxial alignment reported for spherical tactoid assemblies.[30]

The uniformity of the birefringence in crossed polarizers spans several millimeters across in contrast to the conventional dish-cast CNC films where uniformity usually spans only tens of microns[22] (Fig. 2c, d and 3d,e) Moreover, fluorescence confocal polarizing microscopy of the CNC dispersion carried out during the drying confirms that the orientation director and the CNCs are mostly in the direction parallel to the air/suspension interface as bright fluorescence was observed parallel to the edge of capillary (Fig. S6).

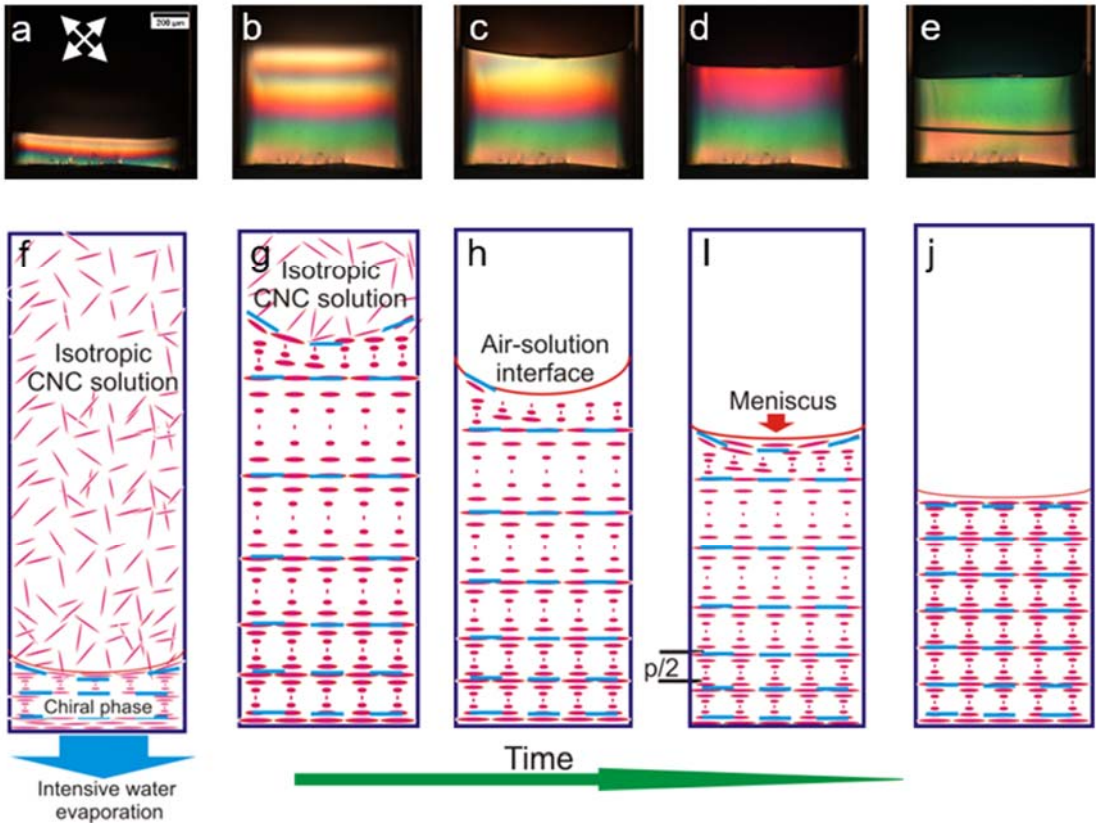

Figure 3. Real time monitoring of drying process using POM (a-e) from the left to the right: 15 min (a), 120 min (b), 128 min (c), 131 min (d), 136 min (e). Polarizer was placed at 45 degree to the capillary edge. The suggested assembly of CNC dispersion in a capillary and its transformation into chiral nematic during drying process (f-j). All images taken along y-axis of capillary (Fig. 1c).

In the end, vertical cracks parallel to the bottom edge of the capillary are formed during the final stage of the film drying process (Figs. 3e, S5b, Video S3). Those cracks are the result of a mismatch of morphology between the twisted structures and the flat rectangular capillary walls. Local stiffness mismatches likely induce these cracks in the film at the final stage in the case of strong adherence of the CNCs to the capillary walls. [42] Such unidirectional crack propagation further confirms the uniform orientation of the nanocrystals parallel to the bottom interface.[20]

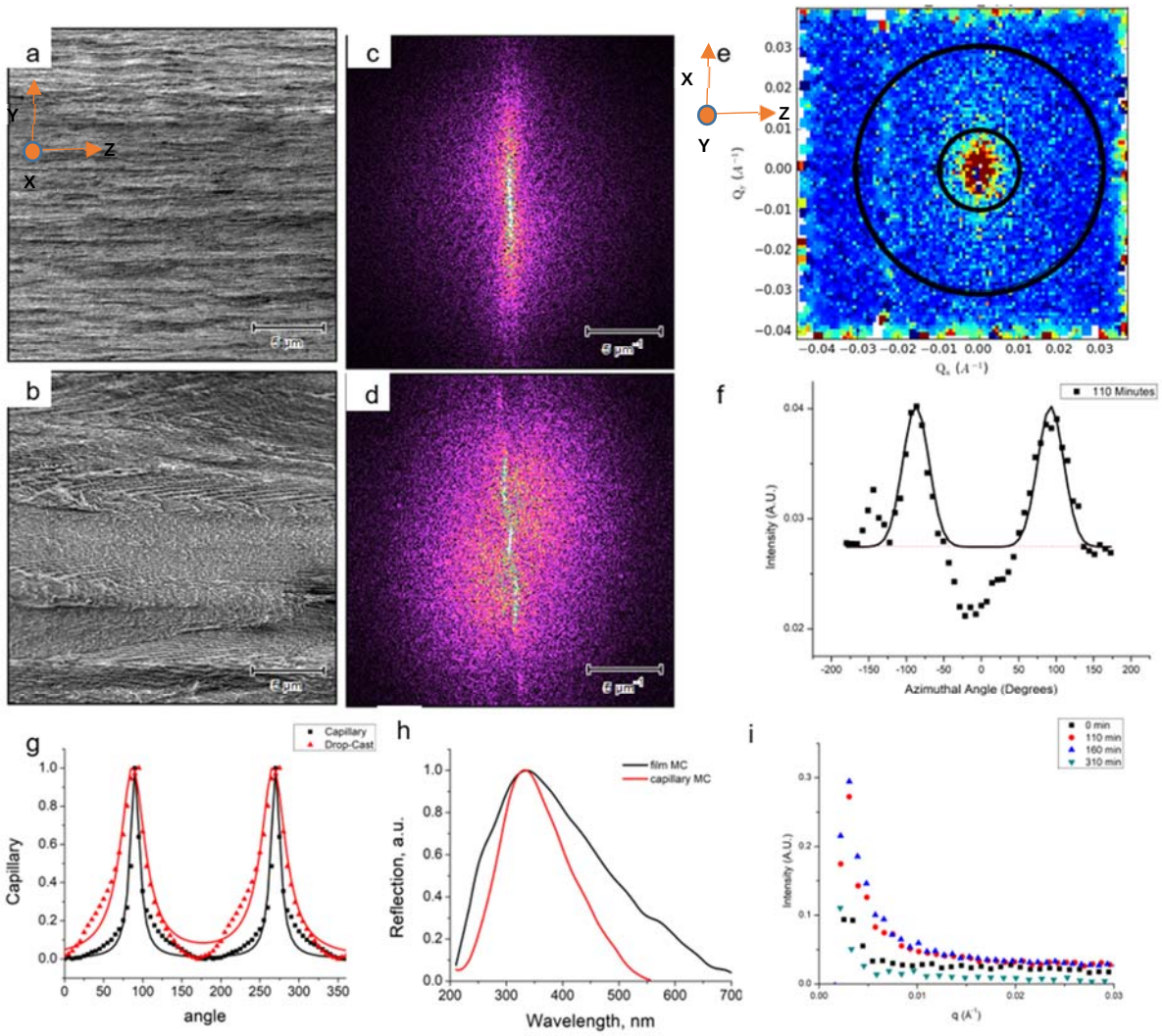

Figure 4. SEM cross-section analysis of (a,c) capillary formed CNC film and (b,d) dish-cast CNC film. (a,b) SEM images are used to generate 2D FFT (c, d). 2D SANS scattering pattern of cellulose nanocrystal suspension in rectangular quartz capillary at 110 min drying (*e*) and corresponding azimuthal SANS intensity distribution (between black circles) with Gaussian fitting (f, low intensity around 0 angle is caused by a beam stopper)). Angular distribution taken from 2D FFT data of solid CNC films with fittings (g). Reflection spectra collected from capillary and dish-cast CNC films (h). Select examples of SANS scattering over drying period (i). Orientations are shown for capillary films (a, c, e).

Overall, the mapping of birefringence shows fast reorientation of the CNC flow at the boundary of anisotropic phase and near-perfect orientation of the optical anisotropy at a microscopic scale with resolution of a few microns (see 2D orientation fields in Fig. S4a,b). Next, the analysis of SEM sections shows the orientation of the chiral domains within capillary-dried and dish-cast CNC films with a high alignment of layered CNC morphology at mesoscale (Figs. 4a, 4b).[43] Moreover, the 2D FFT images show a significant difference in the degree of alignment between the two films with narrower azimuthal distribution for

capillary CNC films (Figs. 4c, 4d). From analysis of the FFT angle distribution (Fig. 4g), we obtained a full width half max of 37 degrees for the dish-cast CNC film versus 14 degrees for the capillary formed film. This value corresponds to very high orientation order parameters of 0.98 that corresponds to the single domain ordering.[44] It should be noted that this method of order parameter determination cannot be directly compared to SANS/SAXS results due to the difference in contrast formation mechanisms. Finally, AFM analysis of the front surfaces of the films indicate a high degree of unidirectional alignment of individual CNCs for the capillary dried films in contrast to the traditional films (Fig. S3a-S3c).

Furthermore, SANS data from contrasted D_2O suspension at the bottom of the capillary at the intermediate drying stage shows sharp increase in scattering intensity at low wavenumber indicating aggregation of the CNC during LC phase formation (within limits of resolution, 10-300 nm) (Figs. 4e, I, S7, S8).[45,46] [47][48] High CNC alignment at a nanoscale is also confirmed by the azimuthal scattering distribution (Fig. 4f). This data shows a full width half max value of ~45 degrees that corresponds to a high orientation order parameter of 0.78. This high orientation order is established very fast (first collection data is 10 min after drying begins) and is consistently constant within the entire drying process of 0.8 ± 0.05 (Fig. S8). This high orientation ordering matches well with recent work on strongly aligned CNC suspensions using strong magnetic field with an order parameter of ~0.73 under a 6.8 T field.[49]

Fig. 4i shows the increase in low angle scattering over time, indicating the formation of larger scattering features. This trend is consistent with the overall increase in scattered intensity over time (Fig. S8a). Interestingly, the overall ordering of the features is quite high (~ 075-0.85 as shown in Fig. S8b) even in the very early stages of drying, but the difference in scattering at perpendicular and parallel orientations grows as the drying proceeds (Figs. S8c-f). This demonstrates a highly preferred alignment direction during the drying process, prior to the final uniaxial drying and compression once the major of the solvent has evaporated, which further improves the orientation of the domains.

Furthermore, the optical reflection spectra as a characteristic of optical performance were analyzed for solid CNC films. As known, the peak wavelength governing the optical Bragg diffraction $\lambda_{max,\infty} = n_{eff}P$ is determined by the pitch P and the effective refractive index $n_{eff} = \frac{n_e+n_o}{2}$, where n_o and n_e are the ordinary and extraordinary refractive indices.[50] The spacing of the layered morphology corresponds well with the pitch of optical reflectance for expected refractive indices within 1.4-1.6. In the case of ideal orientation, the spectral width of the reflection is determined as $\Delta\lambda = \Delta n \cdot P + n \cdot \Delta P$, where $\Delta n = n_e - n_o$. Thus, for a perfectly organized CNC rod-like structures with an estimated Δn of 0.06, the expected spectral width is close to 20 nm.[51] Much larger spectral widths in traditional CNC films suggest significant structural imperfections related to variability of refractive properties and chiral pitches (Fig. 4h, S2g). Common spectral widths of dish-cast CNC films are in the range of 200–500 nm due local heterogeneity of spatial organization, local refractive properties, and orientation.[28,52] The reduced spectral width for capillary-formed CNC films indicates significant reduction of this heterogeneity in comparison with traditional dish-cast films. Indeed, these films show a much narrower spectral width of the reflection band as compared to the drop–cast films, with a full width half max of 242 nm vs 142 nm for the capillary formed film (Fig. 4h). The spectral width observed for capillary-formed solid films is still higher than those observed for small organic molecules based chiral nematics in LC phase due, probably, to additional microscopic defects (e.g., cracks, see Videos S2, S3), introduced by final film drying and which are absent in fluidic LC nematic phases. Adding mediating polymer matrix can mediate the stress release and results in crack initiation suppression in solid CNC-polymer films as will be discussed in future publications. Indeed, in our current efforts, we have already observed that adding xylan matrix to CNC dispersion increases dramatically the mechanical strength and mediates brittle fracture (see Fig. S10).

To confirm that these differences between the capillary-dried and dish-cast CNC films are not dependent on the source of the materials and dimension, both types of the films were fabricated from another source (hard wood (HW)) with longer nanocrystals (210 nm length vs 127 nm length (CNC from microcrystalline cellulose (MC), shown in Fig. 2). We observed that general trends of the formation of CNC films and final morphology were similar for two types of CNCs. For samples from the HW source, the same qualitative differences between

the two fabrication techniques were observed. The optical reflectance (red-shifted to 388 nm due to the expanded helical morphology[33]) of capillary-dried films was narrower by about 20% as compared to dish-cast films (Fig. S2g).

In conclusion, we demonstrated the fabrication of unusually large and uniformly oriented chiral CNC solid films using asymmetrical confined drying conditions within capillary. We suggest that these uniform structures are facilitated by unidirectional CNC suspension flow within a confined capillary environment as supported by unique real-time monitoring of the LC anisotropic phase evolution. This formation process reported here was consistent for the thickness of these capillaries from 50 -100 μm to 500 μm. The resulting chiral CNC films show unusually narrow optical reflectance bands (~40% narrower than conventional dish-casting CNC films reported here) and large area, macroscopically uniform birefringent, chiral regions with unusually high orientation order parameter above 0.8. This simple and effective capillary-confined route for producing high-quality LC CNC materials with controllable uniform morphology and well-identified structural colors adds to the rapidly growing research area of bio-based photonics. Moreover, other confined drying and flow-controlling approaches can be applied to form uniform and larger area (>cm ^{2}) CNC film with enhanced optical reflectance characteristics in future studies (see SI).

EXPERIMENTAL (see more details in SI)

For CNC synthesis, microcrystalline cellulose from Alfa Aesar (designated as MC) was utilized as described elsewhere.[33,53] Two different CNC water dispersions were used to fill the open ended capillaries and one end of the capillary. The length of the filled portion was 15 to 40 mm long in different experiments while the drying process time was 2-6 hours depending on filling conditions. An alternative method of films preparation was performed using 15 mL centrifuge tubes.

The capillary filled with CNC dispersion was placed under the objective of a polarized optical microscope Olympus BX51 operated in the reflection mode with crossed polarizers. Real time monitoring (one frame per 5s) was done over 2-3 hours of film solidification. The CNC formation process was examined using a polarizing microscope (Nikon E600) equipped with

PolScope according to usual procedure. [54,55] The reflection spectra of the CNC film were recorded with an UV-Vis Avantes fiber optic spectrometer using a reflection probe with small tip with the reflection spectra collected by positioning fiber optic probe perpendicular to the film surface. SEM of the dried CNC films was performed on a Zeiss Gemini 500 microscope using a 1 kV accelerating voltage. SEM cross-section of capillary dried films was used for determination of the chiral pitch distribution and orientation order. The morphology of the CNC films peeled from the capillary was examined using AFM (ICON, Bruker) in the soft tapping mode.[56] *SANS* measurements I (q), ($q = \frac{4\pi}{\lambda}\sin\frac{\theta}{2}$) were conducted using the time-of-flight EQ-SANS instrument at the Spallation Neutron Source of Oak Ridge National Laboratory. [57]

Supporting Information: experimental details on sample preparation and characterization; additional images of CNC morphologies at different magnifications; birefringence mapping and fluorescence confocal polarizing microscopy at different stages; SANS data at different stages and intensity and orientation analysis; mechanical analysis of CNC-polymer composite; PolScope and POM videos for accelerated time formation of LC phases.

ACKNOWLEDGMENTS

The research is supported by the Air Force Research Laboratory-Azimuth FA8650-D-16-5404 Grant, Air Force Office of Scientific Research FA9550-17-1-0297, and NSF-CBET 1803495 Award. The authors acknowledge the use of the Spallation Neutron Source, a DOE Office of Science User Facility operated by the Oak Ridge National Laboratory.

REFERENCES

[1] Eichhorn, S. J.; Rahatekar, S. S.; Vignolini, S.; Windle, A H. New horizons for cellulose nanotechnology. *Philos. Trans. Royal Soc. A* **2018,** *376* (2112), 20170200.

[2] Mariano, M.; Kissi, N. E.; Dufresne, A. Cellulose nanocrystals and related nanocomposites: Review of some properties and challenges. *J. Polym. Sci., Part B: Polym. Phys.* **2014,** *52* (12), 791-806.

[3] Hamad, W.Y. *Cellulose Nanocrystals: Properties, Production and Applications.* John Wiley & Sons, Chichester, West Sussex, UK, **2017**.

[4] Yao, K.; Meng, Q.; Bulone, V.; Zhou, Q. Flexible and Responsive Chiral Nematic Cellulose Nanocrystal/Poly(ethylene glycol) Composite Films with Uniform and Tunable Structural Color. *Adv. Mater.* **2017,** *29* (28).

[5] Beck, S.; Bouchard, J.; Berry, R. Controlling the Reflection Wavelength of Iridescent Solid Films of Nanocrystalline Cellulose. *Biomacromolecules* **2011,** *12* (1), 167-172.

[6] P Hyun, P. J.; JungHyun, N.; Christina, S.; German, S. A.; Giusy, S.; Lennart, B.; F., L. J. P. Macroscopic Control of Helix Orientation in Films Dried from Cholesteric Liquid-Crystalline Cellulose Nanocrystal Suspensions. *ChemPhysChem* **2014,** *15* (7), 1477-1484.

[7] Khan Mostofa, K.; Giese, M.; Yu, M.; Kelly Joel, A.; Hamad Wadood, Y.; MacLachlan Mark, J. Flexible Mesoporous Photonic Resins with Tunable Chiral Nematic Structures. *Angew. Chem. Int. Ed.* **2013,** *52* (34), 8921-8924.

[8] Gu, M.; Jiang, C.; Liu, D.; Prempeh, N.; Smalyukh, I. I. Cellulose Nanocrystal/Poly(ethylene glycol) Composite as an Iridescent Coating on Polymer Substrates: Structure-Color and Interface Adhesion. *ACS Appl. Mater. Interfaces* **2016,** *8* (47), 32565-32573.

[9] Lagerwall, J. P. F.; Schütz, C.; Salajkova, M.; Noh, J.; Hyun Park, J.; Scalia, G.; Bergström, L. Cellulose nanocrystal-based materials: from liquid crystal self-assembly and glass formation to multifunctional thin films. *Npg Asia Materials* **2014,** *6*, e80.

[10] Davidson, Z. S.; Huang, Y.; Gross, A.; Martinez, A.; Still, T.; Zhou, C.; Collings, P. J.; Kamien, R. D.; Yodh, A. G. Deposition and drying dynamics of liquid crystal droplets. *Nat. Commun.* **2017,** *8*, 15642.

[11] Mu, X.; Gray, D. G. Droplets of cellulose nanocrystal suspensions on drying give iridescent 3-D “coffee-stain” rings. *Cellulose* **2015,** *22* (2), 1103-1107.

[12] Li, Y.; Prince, E.; Cho, S.; Salari, A.; Mosaddeghian Golestani, Y.; Lavrentovich, O. D.; Kumacheva, E. Periodic assembly of nanoparticle arrays in disclinations of cholesteric liquid crystals. *Proc Natl Acad Sci U S A* **2017,** *114* (9), 2137-2142.

[13] Li, Y.; Jun-Yan Suen, J.; Prince, E.; Larin, E. M.; Klinkova, A.; Thérien-Aubin, H.; Zhu, S.; Yang, B.; Helmy, A. S.; Lavrentovich, O. D.; Kumacheva, E. Colloidal cholesteric liquid crystal in spherical confinement. *Nat. Commun.* **2016,** *7*, 12520.

[14] Hirai, A.; Inui, O.; Horii, F.; Tsuji, M. Phase Separation Behavior in Aqueous Suspensions of Bacterial Cellulose Nanocrystals Prepared by Sulfuric Acid Treatment. *Langmuir* **2009,** *25* (1), 497-502.

[15] Prinsen, P.; van der Schoot, P. Shape and director-field transformation of tactoids. *Phys. Rev. E* **2003,** *68* (2), 021701.

[16] Revol, J.-F.; Godbout, L.; Dong, X.-M.; Gray, D. G.; Chanzy, H.; Maret, G. Chiral nematic suspensions of cellulose crystallites; phase separation and magnetic field orientation. *Liq. Cryst.* **1994,** *16* (1), 127-134.

[17] Nan, F.; Chen, Q.; Liu, P.; Nagarajan, S.; Duan, Y.; Zhang, J. Iridescent graphene/cellulose nanocrystal film with water response and highly electrical conductivity. *RSC Adv.* **2016,** *6* (96), 93673-93679.

[18] Wang, Y.; Qi, W.; Xing, R.; Xing, Q.; Su, R.; He, Z. Capillary Flow-Driven, Hierarchical Chiral Self-Assembly of Peptide Nanohelix Arrays. *Adv. Mater. Interfaces* **2017,** *4* (19), 1700514.

[19] Wang, P. X.; MacLachlan, M. J. Liquid crystalline tactoids: ordered structure, defective coalescence and evolution in confined geometries. *Philos. Trans. Royal Soc. A* **2018,** *376* (2112), 20170042.
[20] Gray, D. G.; Mu, X. Chiral Nematic Structure of Cellulose Nanocrystal Suspensions and Films; Polarized Light and Atomic Force Microscopy. *Materials* **2015,** *8* (11), 7873-7888.
[21] Honorato-Rios, C.; Kuhnhold, A.; Bruckner, J. R.; Dannert, R.; Schilling, T.; Lagerwall, J. P. F. Equilibrium Liquid Crystal Phase Diagrams and Detection of Kinetic Arrest in Cellulose Nanocrystal Suspensions. *Front. Mater.* **2016,** *3* (21).
[22] Wang, P.-X.; Hamad, W. Y.; MacLachlan, M. J. Structure and transformation of tactoids in cellulose nanocrystal suspensions. *Nat. Commun.* **2016,** *7*, 11515.
[23] Beck-Candanedo, S.; Roman, M.; Gray, D. G. Effect of Reaction Conditions on the Properties and Behavior of Wood Cellulose Nanocrystal Suspensions. *Biomacromolecules* **2005,** *6* (2), 1048-1054.
[24] Kang, K.; Dhont, J. K. Glass transition in suspensions of charged rods: structural arrest and texture dynamics. *Phys. Rev. Lett.* **2013,** *110* (1), 015901.
[25] Gençer, A.; Schütz, C.; Thielemans, W. Influence of the Particle Concentration and Marangoni Flow on the Formation of Cellulose Nanocrystal Films. *Langmuir* **2017,** *33* (1), 228-234.
[26] Tran, A.; Hamad, W. Y.; MacLachlan, M. J. Tactoid Annealing Improves Order in Self-Assembled Cellulose Nanocrystal Films with Chiral Nematic Structures. *Langmuir* **2018,** *34* (2), 646-652.
[27] Tatsumi, M.; Teramoto, Y.; Nishio, Y. Different orientation patterns of cellulose nanocrystal films prepared from aqueous suspensions by shearing under evaporation. *Cellulose* **2015,** *22* (5), 2983-2992.
[28] Ličen, M.; Majaron, B.; Noh, J.; Schütz, C.; Bergström, L.; Lagerwall, J.; Drevenšek-Olenik, I. Correlation between structural properties and iridescent colors of cellulose nanocrystalline films. *Cellulose* **2016,** *23* (6), 3601-3609.
[29] Kelly, J. A.; Yu, M.; Hamad, W. Y.; MacLachlan, M. J. Large, Crack-Free Freestanding Films with Chiral Nematic Structures. *Adv. Opt. Mater.* **2013,** *1* (4), 295-299.
[30] Parker, R. M.; Frka-Petesic, B.; Guidetti, G.; Kamita, G.; Consani, G.; Abell, C.; Vignolini, S. Hierarchical Self-Assembly of Cellulose Nanocrystals in a Confined Geometry. *ACS Nano* **2016,** *10* (9), 8443-8449.
[31] Frka-Petesic, B.; Guidetti, G.; Kamita, G.; Vignolini, S. Controlling the Photonic Properties of Cholesteric Cellulose Nanocrystal Films with Magnets. *Adv. Mater.* **2017,** *29* (32) doi: 10.1002/adma.201701469.
[32] Chen, Q.; Liu, P.; Nan, F.; Zhou, L.; Zhang, J. Tuning the Iridescence of Chiral Nematic Cellulose Nanocrystal Films with a Vacuum-Assisted Self-Assembly Technique. *Biomacromolecules* **2014,** *15* (11), 4343-4350.
[33] Korolovych, V. F.; Cherpak, V.; Nepal, D.; Ng, A.; Shaikh, N. R.; Grant, A.; Xiong, R.; Bunning, T. J.; Tsukruk, V. V. Cellulose nanocrystals with different morphologies and chiral properties *Polymer* **2018,** *145*, 334-347.
[34] Keita, E.; Koehler, S. A.; Faure, P.; Weitz, D. A.; Coussot, P. Drying kinetics driven by the shape of the air/water interface in a capillary channel. *Eur. Phys. J. E* **2016,** *39* (2), 23.
[35] Keita, E.; Koehler, S. A.; Faure, P.; Weitz, D. A.; Coussot, P. *Eur. Phys. J. E* **2016,** *39*, 23.
[36] Fernandes Susete, N.; Almeida Pedro, L.; Monge, N.; Aguirre Luis, E.; Reis, D.; de Oliveira Cristiano, L. P.; Neto António, M. F.; Pieranski, P.; Godinho Maria, H. Mind the Microgap in Iridescent Cellulose Nanocrystal Films. *Adv. Mater.* **2016,** *29* (2), 1603560.
[37] Dumanli Ahu, G.; Kamita, G.; Landman, J.; van der Kooij, H.; Glover Beverley, J.; Baumberg Jeremy, J.; Steiner, U.; Vignolini, S. Controlled, Bio-inspired Self-Assembly of Cellulose-Based Chiral Reflectors. *Adv. Opt. Mater.* **2014,** *2* (7), 646-650.
[38] Oh, D. X.; Cha, Y. J.; Nguyen, H.-L.; Je, H. H.; Jho, Y. S.; Hwang, D. S.; Yoon, D. K. Chiral nematic self-assembly of minimally surface damaged chitin nanofibrils and its load bearing functions. *Sci. Rep.* **2016,** *6*, 23245.

[39] Kong, Y. L.; Boulogne, F.; Kim, H.; Nunes, J.; Feng, J.; Stone, H. A. Deposition of Quantum Dots in a Capillary Tube. *Langmuir* **2015,** *31* (45), 12560-12566.
[40] Parker Richard, M.; Guidetti, G.; Williams Cyan, A.; Zhao, T.; Narkevicius, A.; Vignolini, S.; Frka-Petesic, B. The Self-Assembly of Cellulose Nanocrystals: Hierarchical Design of Visual Appearance. *Adv. Mater.* **2017,** *30* (19), 1704477.
[41] Orts, W. J.; Godbout, L.; Marchessault, R. H.; Revol, J. F. Enhanced Ordering of Liquid Crystalline Suspensions of Cellulose Microfibrils: A Small Angle Neutron Scattering Study. *Macromolecules* **1998,** *31* (17), 5717-5725.
[42] Thiery, J.; Keita, E.; Rodts, S.; Courtier Murias, D.; Kodger, T.; Pegoraro, A.; Coussot, P. Drying kinetics of deformable and cracking nano-porous gels. *Eur. Phys. J. E* **2016,** *39* (12), 117.
[43] Majoinen, J.; Kontturi, E.; Ikkala, O.; Gray, D. G. SEM imaging of chiral nematic films cast from cellulose nanocrystal suspensions. *Cellulose* **2012,** *19* (5), 1599-1605.
[44] Chowdhury, R. A.; Peng, S. X.; Youngblood, J. Improved order parameter (alignment) determination in cellulose nanocrystal (CNC) films by a simple optical birefringence method. *Cellulose* **2017,** *24* (5), 1957-1970.
[45] Liu, Y.; Stoeckel, D.; Gordeyeva, K.; Agthe, M.; Schütz, C.; Fall, A. B.; Bergström, L. Nanoscale Assembly of Cellulose Nanocrystals during Drying and Redispersion. *ACS Macro Lett.* **2018,** *7* (2), 172-177.
[46] Uhlig, M.; Fall, A.; Wellert, S.; Lehmann, M.; Prévost, S.; Wågberg, L.; von Klitzing, R.; Nyström, G. Two-Dimensional Aggregation and Semidilute Ordering in Cellulose Nanocrystals. *Langmuir* **2016,** *32* (2), 442-450.
[47] Schütz, C.; Agthe, M.; Fall, A. B.; Gordeyeva, K.; Guccini, V.; Salajková, M.; Plivelic, T. S.; Lagerwall, J. P. F.; Salazar-Alvarez, G.; Bergström, L. Rod Packing in Chiral Nematic Cellulose Nanocrystal Dispersions Studied by Small-Angle X-ray Scattering and Laser Diffraction. *Langmuir* **2015,** *31* (23), 6507-6513.
[48] Mao, Y.; Liu, K.; Zhan, C.; Geng, L.; Chu, B.; Hsiao, B. S. Characterization of Nanocellulose Using Small-Angle Neutron, X-ray, and Dynamic Light Scattering Techniques. *J. Phys. Chem. B* **2017,** *121* (6), 1340-1351.
[49] Guccini, V.; Trushkina, Y.; Nagy, G.; Schutz, C.; Salar-Alvarez, G. presented at MRS, Phoenix, AZ, USA, April, **2018**.
[50] Belyakov, V. A.; Dmitrienko, V. E. *Optics of Chiral Liquid Crystals*. Harwood, New York, **1989**.
[51] Frka-Petesic, B.; Sugiyama, J.; Kimura, S.; Chanzy, H.; Maret, G. Negative Diamagnetic Anisotropy and Birefringence of Cellulose Nanocrystals. *Macromolecules* **2015,** *48* (24), 8844-8857.
[52] Haywood, A. D.; Davis, V. A. Effects of liquid crystalline and shear alignment on the optical properties of cellulose nanocrystal films. *Cellulose* **2017,** *24* (2), 705-716.
[53] Shopsowitz, K. E.; Kelly, J. A.; Hamad, W. Y.; MacLachlan, M. J. Biopolymer Templated Glass with a Twist: Controlling the Chirality, Porosity, and Photonic Properties of Silica with Cellulose Nanocrystals. *Adv. Funct. Mater.* **2013,** *24* (3), 327-338.
[54] Oldenbourg, R.; Mei, G. New polarized light microscope with precision universal compensator. *J. Microsc.* **1995,** *180* (Pt 2), 140-147.
[55] Zhou, S.; Sokolov, A.; Lavrentovich, O. D.; Aranson, I. S. Living liquid crystals. *Proc. Natl. Acad. Sci. U.S.A* **2014,** *111* (4), 1265.
[56] McConney, M. E.; Singamaneni, S.; Tsukruk, V. V. Probing Soft Matter with the Atomic Force Microscopies: Imaging and Force Spectroscopy. *Polymer Reviews* **2010,** *50* (3), 235-286.
[57] Zhao, J. K.; Gao, C. Y.; Liu, D. The Extended Q-Range Small-Angle Neutron Scattering Diffractometer at the SNS. *J. Appl. Crystallogr.* **2010,** 43, 1068-1077.

TOC

Cherpak et al.
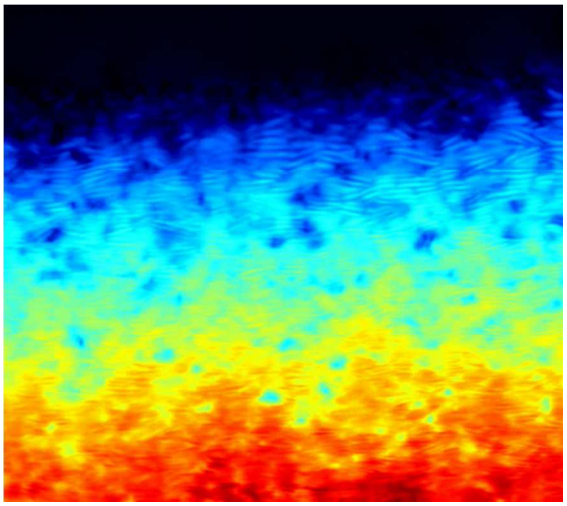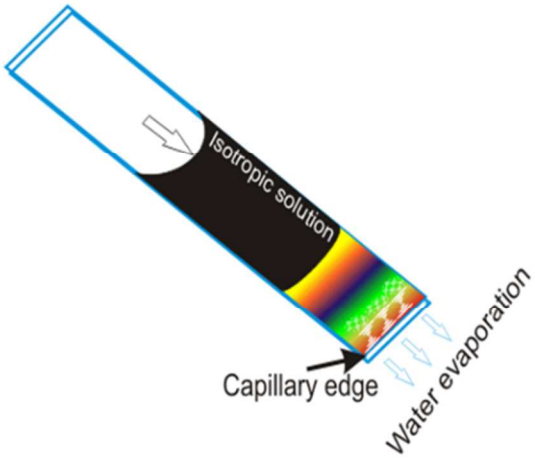
We showed large area uniformly aligned chiral photonic bioderived films from a liquid crystal phase formed by a cellulose nanocrystal (CNC) suspension placed in a thin capillary.